Multisegmented FeCo/Cu Nanowires: Electrosynthesis, Characterization, and Magnetic Control of Biomolecule Desorption

Author(s):
Özkale, Berna; Shamsudhin, Naveen; Chatzipirpiridis, George; Hoop, Marcus; Gramm, Fabian; Chen, Xiangzhong; Marti, Xavi; Sort, Jordi; Pellicer, Eva; Pané, Salvador

Publication date:
2015-04-08

Permanent link:
https://doi.org/10.3929/ethz-a-010625313

Originally published in:
ACS Applied Materials & Interfaces 7(13), https://doi.org/10.1021/acsami.5b01143

Multisegmented FeCo/Cu nanowires: electrosynthesis, characterization and magnetic control of biomolecule desorption

Berna Özkale,[§] Naveen Shamsudhin,[§] George Chatzipirpiridis,[§] Marcus Hoop,[§] Fabian Gramm,[□] Xiangzhong Chen,[§] Xavi Martí,[ξ] Jordi Sort,[‡,] Eva Pellicer,[†] and Salvador Pané[§,*]*

[§] Multi-Scale Robotics Lab (MSRL), Institute of Robotics & Intelligent Systems (IRIS), ETH Zürich, Zürich 8092, Switzerland

[□] Scientific Center for Optical and Electron Microscopy (ScopeM), ETH Zürich, Zürich 8093, Switzerland

[ξ] Department of Spintronics and Nanoelectronics, Institute of Physics ASCR, v.v.i., Cukrovarnická 10, 162 53 Praha 6, Czech Republic

[‡] Institució Catalana de Recerca i Estudis Avançats (ICREA) and Departament de Física, Universitat Autònoma de Barcelona, Campus UAB, Bellaterra, 08193 (Spain)

[†] Departament de Física, Facultat de Ciències, Universitat Autònoma de Barcelona, Campus UAB, Bellaterra 08193, Spain

* Corresponding authors: sort.jordi@uab.cat, vidalp@ethz.ch

ABSTRACT

In this paper, we report on the synthesis of FeCo/Cu multisegmented nanowires by means of pulse electrodeposition in nanoporous anodic aluminum oxide arrays supported on silicon chips. By adjusting the electrodeposition conditions, such as the pulse scheme and the electrolyte, alternating segments of Cu and ferromagnetic FeCo alloy can be fabricated. The segments can be built with a wide range of lengths (15 – 150 nm) and exhibit a close-to-pure composition (Cu or FeCo alloy) as suggested by EDX mapping results. The morphology and the crystallographic structure of different nanowire configurations have been assessed thoroughly concluding that Fe, Co and Cu form solid solution. Magnetic characterization using vibrating sample magnetometry and magnetic force microscopy reveals that by introducing non-magnetic Cu segments within the nanowire architecture, the magnetic easy axis can be modified and the reduced remanence can be tuned to the desired values. The experimental results are in agreement with the provided simulations. Furthermore, the influence of nanowire magnetic architecture on the magnetically triggered protein desorption is evaluated for three types of nanowires: Cu, FeCo and multisegmented $FeCo_{15\ nm}/Cu_{15\ nm}$. The application of an external magnetic field can be used to enhance the release of proteins on-demand. For fully magnetic FeCo nanowires the applied oscillating field increased protein release by 83%, whereas this was found to be 45% for multisegmented $FeCo_{15\ nm}/Cu_{15\ nm}$ nanowires. Our work suggests that a combination of arrays of nanowires with different magnetic configurations could be used to generate complex substance concentration gradients or control delivery of multiple drugs and macromolecules.

Keywords: multisegmented nanowires, template-assisted electrodeposition, tunable magnetic properties, magnetically triggered release

1. INTRODUCTION

Magnetic nanowires (NWs) have recently attracted considerable attention for their use in data storage devices and magnetic logic circuits,[1,2] sensors,[3] biofuel cells,[4] bioreactors,[5] or as antibiofouling platforms.[6] An important class of NWs for applications in magnetic devices are segmented NWs (SNWs). The possibility to build these nanoarchitectures by combining ferromagnetic (FM) and non-magnetic (NM) segments enables fine-tuning of their magnetic properties such as coercive field, saturation magnetization, and remanence, or the orientation of the magnetic easy axis.[7-9] Despite the inherent flexibility of their functional properties, the production of SNWs is limited to only a few fabrication methods, all of them based on the use of organic[10,11] or inorganic templates[12] for their growth. In general, the most prevalent approach for synthesizing NWs is electrochemical deposition in nanoporous anodic aluminum oxide (AAO) membranes. These templates offer great flexibility in terms of NW dimensionality, since pores of different length and diameter can be readily formed. Hence, this method is convenient for obtaining customized magnetic properties as a function of the pore size. Based on this approach, NW segmentation is achieved by sequential electrodeposition using different electrolytes[13] or in a single bath by swapping between two different current densities (or electrochemical potentials).[14] Although the latter strategy is the most convenient methodology, because it significantly abridges the fabrication sequence, there are still challenges to overcome. For example, one of the main difficulties is to achieve segments in which the FM and the NM segments are compositionally pure, i.e., the presence of the NM component should be minimized in the FM layer, and vice versa. To achieve this, there should be a sufficiently large difference between the electrochemical potentials corresponding to the NM and the FM parts.[15] The use of

additives such as complexing agents can aid this process, although this is not always beneficial since undesired crystallization processes or texture changes may occur.[16] Other challenges in the fabrication of SNWs are related to lattice mismatch between subsequent layers due to changes in the segment crystal structure, which, in turn can lead to a poor adhesion between the layers or uneven morphological growth.[17]

In this paper, we present the fabrication of FeCo/Cu multisegmented nanowires (MSNWs) obtained from a single electrolyte in AAO templates formed on silicon substrates. FeCo/Cu MSNWs are attractive due to the higher saturation magnetization (around 2.4 T) exhibited by the FeCo system.[18] Moreover, FeCo thin films have been recently reported to exhibit giant magnetostriction,[19] and giant magnetoresistance when combined with Cu segments into multilayered thin films.[20] The influence of non-magnetic Cu segments on the magnetization of the NWs was primarily simulated, and experimentally verified and investigated in detail by vibrating sample magnetometer (VSM) and magnetic force microscopy (MFM). The results demonstrate that magnetic easy axis can be reversed using the appropriate NW architecture. Finally, the effect of NW segmentation on the on-demand macromolecule release was studied with the application of an external oscillating magnetic field. For this purpose, a model macromolecule, bovine serum albumin (BSA), was adsorbed on the NW surface and a release assay was realized with and without magnetic field. The results suggest that protein release can be tailored by both NWs magnetic structure and the external magnetic fields. This approach is an attractive route for regulating macromolecular adsorption using magnetic nanoagents and serves as a way to produce sophisticated devices for the production of complex concentration gradients of macromolecules.

2. EXPERIMENTAL SECTION

2.1. Synthesis of FeCo/Cu MSNWs

FeCo/Cu MSNWs were fabricated electrochemically from a single aqueous bath using anodized alumina templates. For this purpose a previously optimized one-step anodization procedure was utilized.[21] Briefly, Ti/Au/Al coated Si/SiO_2 chips were anodized in 0.3 M oxalic acid at a potential of +60 V. The anodized chips were subjected to chemical etching using 5 % (v/v) phosphoric acid in order to widen the pores to the desired value of 100 nm. The area of anodization and subsequent electrodeposition was 0.5 cm^2. FeCo/Cu MSNWs were grown by pulse electrodeposition in previously fabricated templates using a sulphate-chloride based bath (Table 1). All chemicals were acquired from Sigma-Aldrich with analytical purity and were used as received. Ascorbic acid was used to prevent the oxidation of Fe(II) to Fe(III). Glycine acted as a complexing agent in order to minimize the formation of metal hydroxides and oxohydroxides at the working electrode. Ammonium chloride, boric acid and sodium saccharinate were employed as conducting salt, pH buffer and stress reducer, respectively. Polyethylene glycol (PEG) with a molecular weight (MW) of 400 g mol^{-1} served as a surfactant and leveler. All electrochemical experiments were performed by an Autolab PGSTAT302N potentiostat at room temperature. A two-electrode electrochemical cell was used where a platinized titanium sheet functioned as the counter electrode. During electrodeposition, the bath was stirred with a constant speed (300 rpm) and N_2 was purged through the solution to remove gas bubbles from the sample surface. Ternary alloy NWs were obtained potentiostatically at a fixed potential. FeCo/Cu MSNWs were grown potentiostatically by alternating the potential between -1.8 V and -0.7 V for the FeCo- and Cu-rich segments, respectively. The pulse times were varied between 0.5 to 4 s for FeCo- and 15 to 120 s for Cu-rich segments in order to obtain a range of segment lengths from 15 nm to 150 nm for both. The total length of the NWs was always kept at

approximately 1.5 μm for all the conditions. An overview of the fabrication process is shown schematically in Figure 1(a).

2.2. Material Characterization

Morphology of the resulting NWs was studied by scanning electron microscopy (SEM, Zeiss ULTRA 55), transmission electron microscopy (TEM, FEI F30), and scanning transmission electron microscopy (STEM, FEI F30). The composition and crystallographic structure of the NWs was analyzed by energy dispersive X-ray analysis (EDX) and X-ray diffraction (XRD, Bruker AXS D8 Advance, Cu K_α) using a step size of 0.02° and step time of 10 s, respectively. Distribution of elements along the NW was studied by EDX mapping using STEM (Hitachi HD-2700). Cross-sectional views of the NWs after growth were acquired by a focused ion beam (FIB) coupled with SEM (NVision 40 Zeiss). The local crystallographic structure was also studied by selected area electron diffraction (SAED). Magnetic characterization was performed on experimentally grown NWs using a vibrating sample magnetometer (VSM, Princeton Measurements Corporation) and magnetic force microscopy (MFM, Bruker Dimension V AFM) and the results were compared to the simulations. For the VSM measurements, four different types of MSNWs were analyzed, which were chosen as $FeCo_{15\ nm}/Cu_{15\ nm}$, $FeCo_{15\ nm}/Cu_{100\ nm}$, $FeCo_{100\ nm}/Cu_{15\ nm}$, $FeCo_{100\ nm}/Cu_{100\ nm}$, and non-segmented FeCo-rich (95 %) ternary alloy NWs. MFM measurements were performed on $FeCo_{150\ nm}/Cu_{150\ nm}$ and FeCo-rich NWs using a MESP cantilever with a CoCr tip coating with an approximate nominal coercivity of 400 Oe. The surface topography information and MFM images were acquired using the following procedure. The cantilever was first scanned over the sample in intermittent contact operation to reveal the topography of individual NWs followed by scanning at a fixed height of 50 nm above the

recorded topography and recording the deflection of the cantilever due to magnetostatic tip-sample interactions.

2.3. Simulations

The magnetization loops of the individual MSNWs were simulated using the micromagnetic simulation package Nmag,[22] and the influence of dipolar interactions between the magnetic segments was studied. The easy-axis of magnetization of these NWs can clearly be tuned using the thickness of the magnetic and non-magnetic segments as control parameters.

2.4. Magnetically Triggered Release Experiments

The on-demand protein release properties of FeCo/Cu MSNWs were studied using an assay reported elsewhere.[6] Prior to protein release experiments, the alumina template was removed using 10 wt % NaOH at 75 °C. Then, the resulting freestanding NWs on silicon chips were incubated for 1 hour in phosphate buffered saline (PBS, Gibco) solution containing 1 mg/ml BSA (Sigma). At the end of the incubation time, samples were removed and washed in PBS briefly to remove non-adsorbed BSA and were placed in clean glass beakers. Fresh PBS (2 ml) was added and BSA release was performed for 15 minutes after which the solution was removed and analyzed by a standard Bradford assay (Thermo Scientific) for BSA content. For this purpose, 150 µl of reagent and 150 µl of sample solution was added in a transparent 96 well plate and incubated for 10 minutes at room temperature. Absorption measurements were conducted using a spectrophotometer (TECAN, Infinite 200 PRO) at a wavelength of 595 nm. The standard curve was prepared using the BSA standards provided with the assay kit and the same protocol. The effect of magnetic segmentation within the FeCo/Cu MSNWs on the on-

demand release performance was studied using three types of NWs, namely Cu-rich, FeCo-rich, and $FeCo_{15\ nm}/Cu_{15\ nm}$ NWs. For this purpose, the samples for each NW type were divided into two groups and one group was subjected to an external oscillating magnetic field of 4 mT with 10 Hz, whereas the second group did not receive any. Each condition was replicated four times. A uniform magnetic field was applied using a home-built electromagnetic setup consisting of two coils with FeCo cores connected to voltage amplifiers (AE Techron 7224), and controlled by a Labview program.

3. RESULTS AND DISCUSSION

3.1. Composition, Morphology and Structural Characterization

In order to optimize the purity of FeCo and Cu segments, the effect of deposition potential on composition was studied. For this purpose, ternary alloy NWs were grown at a range of potentials, and the resulting composition was analyzed by EDX (Figure 1 (b)). As expected, the Cu content in the NWs decreased while FeCo amount increased with more negative potentials. Potentials more positive than -0.7 V resulted in non-homogeneous Cu-rich NWs with no significant improvement in the composition. In all the range of potentials, an increase of Co was observed when depositing at more negative potentials. The Fe content was also increased up to -1.4 V but was decreased slightly onwards. For all studied deposition potentials the Co content was always higher than Fe. Interestingly, FeCo codeposition is usually anomalous,[23] which was not observed in our case. Additionally, potentials more negative than -1.8 V did not significantly change FeCo amount in the NW. Therefore, the growth potentials of FeCo- and Cu-rich segments were chosen as -1.8 V and -0.7 V, respectively. The FeCo alloy obtained at -1.8 V exhibits a Co content of ~65 at%, a composition for which these alloys show high values of

magnetostriction once annealed.[19] During the optimization of the bath, it was observed that the potentiostatic mode offers better uniformity and less deviation in segment size as opposed to the galvanostatic mode. This is probably due to slight changes in the deposition area of the homemade AAO templates. The addition of a surfactant to the bath such as PEG_{400} and the optimum complexing agent (glycine) concentration were found to be crucial. In the absence of glycine, the NWs exhibited an incomplete, non-homogeneous structure probably due to the formation of metal oxyhydroxides and hydroxides (see supporting information (SI), Figure S1). Apart from its complexing effect, glycine can act as a pH buffer.[23] The presence of PEG_{400} rendered homogeneous MSNWs with a smoother morphology. It is reported that polyoxyethylene-based surfactants such as PEG exert a leveling function especially in Cu electrodeposition.[24] PEG in the presence of chlorides exhibits a suppression behavior in Cu deposition, especially at the bottom of trenches and vias, thus enhancing a careful control on Cu growth. Figure 1(c) provides a cross-sectional view of the resulting optimized NWs in the AAO template showing that the MSNWs grow homogenously within the pores.

FeCo/Cu MSNWs with different segment sizes (denoted by the subscript) ranging from 15 nm to 150 nm could be obtained by varying the pulse time between 0.5 to 4 s for FeCo and between 15 to 120 s for Cu rich segments. Figure 2 shows selected images of $FeCo_{15\ nm}/Cu_{15\ nm}$ (a), $FeCo_{15\ nm}/Cu_{100\ nm}$ (b), $FeCo_{100\ nm}/Cu_{15\ nm}$ (c), and $FeCo_{100\ nm}/Cu_{100\ nm}$ (d) MSNWs. The total number of segments along the MSNWs varied from 64 to 8 depending on the selected condition. The FeCo and Cu segments can be clearly distinguished for all the NWs thanks to their bright/dark contrast, respectively. Namely, the bright segments correspond to Cu-rich and the dark segments to FeCo-rich regions. In general the NWs are homogeneous and exhibit a smooth morphology with consistent segment sizes. For the case of small FeCo and large Cu segments (Figure 2 (b)),

highly defective junctions were noticed due to the long size of Cu segments. This could be related to the low concentration of Cu in the electrolyte resulting from depletion of Cu ions during deposition. This has been observed in other systems such as pure Fe. Haehnel et al. report that long NWs exhibit a compact and dense surface morphology only at the lower parts. In contrast, the upper regions were discontinuous, irregular and thinner.[25, 26] Additionally, the inhomogeneous growth of Cu for large segments was also found to be deleterious for the subsequent deposition of FeCo segments. Therefore, the maximum pulse time for Cu was restricted to 120 s. This was not the case for large FeCo segments in which such defects were not observed (Figure 2 (c)).

The distribution of Fe, Co and Cu elements in the MSNWs was studied by EDX mapping. Figure 3 shows the STEM image of a selected area for a $FeCo_{15\ nm}/Cu_{15\ nm}$ MSNW (Figure 3 (a)) and the corresponding EDX maps for Co, Fe, and Cu (Figure 3 (b)-(d)). A clear differentiation of Fe, Co and Cu distribution can be observed where both FeCo- and Cu-rich segments are easily distinguished. As expected, the bright segments are rich in Cu whereas the dark segments are rich in Fe and Co. Although the FeCo and Cu segments seem to be equal in length according to Figure 3 (a), EDX mapping shows that the Cu-rich segments are actually shorter than the FeCo-rich segments. This discrepancy comes from the fact that the heavier element Cu displays higher contrast than FeCo in the STEM micrograph (Figure 3 (a)). Instead, EDX mapping provides direct information on element distribution, resulting in a more precise estimation of segment size. The compositional EDX mapping suggests that both FeCo and Cu segments are almost completely pure. Only small intermixing was observed probably due to the complexation effect of glycine.

XRD patterns for both MSNWs and ternary alloy NWs fabricated at different potentials are given in Figure 3 (e). The ternary alloy NWs fabricated at -0.7 V show the characteristic face-centered-cubic (fcc) reflections due to the high content of Cu (95 %) in the NW obtained using this potential. The (111) fcc peak located at 2θ = 43.5º remains visible in the sample grown at -1.1 V but with lower intensity due to the lower Cu content (~ 25%). Clear peaks corresponding to fcc Co-based alloy and body-centered-cubic (bcc) Fe-based alloy are present in the samples grown at -1.1 V and -1.8 V (and in the MSNWs). The slight shifts towards higher angles compared to the tabulated angular positions for pure fcc-Co and bcc-Fe phases indicate that all three elements form solid solutions in these phases. The different relative intensities of these peaks in the different samples can be understood as a consequence of their dissimilar composition. In addition, increasing the growth potential from -1.1 V to -1.8 V causes a shift in the fcc (111) peak (located at approximately 2θ = 45º) toward higher angles. This is probably due to the higher content of Co in the deposit grown at higher potential, which results in a relative change in the amount of fcc-Co and bcc (Fe-based) phases, as well as changes in the lattice parameters. Interestingly, NWs grown at -1.8 V, a peak appears at 2θ = 40.7º, which matches the position of the (100) reflection of a Co-rich hcp phase. The pattern obtained for $FeCo_{15\ nm}/Cu_{15\ nm}$ MSNWs (Figure 3 (e)) shows a similar behavior to the ternary alloy grown at -1.8 V, indicating that the Cu segments (grown at -0.7 V) are probably too short to give a significant signal in the XRD pattern. The values of cell parameters, crystallite sizes and microstrains, as determined from Rietveld refinements of the XRD data, are shown in the SI (Table S1). The crystallite size ranges from about 30 to 60 nm, depending on the sample and crystallographic phase. The SAED pattern of the MSNWs (Figure 3 (f)) shows that the NWs are polycrystalline where multiple rings corresponding to the same phases as determined from XRD

are observed. It should be noted that the fcc (200) reflection is low in intensity and is dependent on the NW location, suggesting that the contribution from fcc-Cu is very low over the entire sample. These findings are also supported with the HRTEM image shown in Figure 3 (g) where the polycrystalline structure is again well evident.

3.2. Magnetic Characterization

3.2.1. Micromagnetic Simulations of NWs with variable segment lengths

The micromagnetic simulations of the hysteresis loops for individual nanowires were performed using the Nmag code, and the results are shown in Figure 4 (a, b). The geometry of each nanowire was set to be 100 nm in diameter and 1500 nm in length. Six different variants in their magnetic/non-magnetic segment sizes were compared. The average cell size for the simulations was around 3 nm, and the saturation magnetization M_s is 1583 emu/cm^3 calculated for FeCo (55% Fe, 45% Co). The magnetocrystalline anisotropy was neglected because of the polycrystallinity of the NWs (as seen in Figure 3 (g)), which reduces the overall effective anisotropy and the expected soft ferromagnetic behavior. The exchange constant considered for FeCo alloy is $A = 2 \times 10^{-11}$ J/m.[27] The precession term was switched off to speed up the simulations and an energy minimization algorithm was used to compute the hysteresis loops. As expected, the $FeCo_{1500\ nm}/Cu_{0\ nm}$ NW (labeled as FeCo-rich) has the magnetic easy axis (the preferred orientation of magnetization) along its length owing to its large shape anisotropy. In addition, both the $FeCo_{100\ nm}/Cu_{15\ nm}$ and the $FeCo_{100\ nm}/Cu_{100\ nm}$ MSNWs have their easy axes along their length. Conversely, the MSNWs variants with extremely thin magnetic segments (thickness of 15 nm) have a small segment aspect ratio, which favors an overall radial magnetization of the NW. Interestingly, the $FeCo_{15\ nm}/Cu_{15\ nm}$ MSNW exhibits a reduced radial

susceptibility when compared to the $FeCo_{15\ nm}/Cu_{100\ nm}$ MSNW, because the nonmagnetic segment is insufficiently thick to avoid the influence of the magnetostatic interaction between the FM segments of the NW.

3.2.2. VSM Measurements of the NWs

Magnetic hysteresis loops of the FeCo/Cu MSNWs measured at room temperature along the parallel and perpendicular directions with respect to the NW long axis are compared in Figure 4 (c, d). The measured coercivity and reduced remanence (M_r/M_s) values are shown in Table 2.

The trends observed in the experimental measurements for the ensemble of NWs agree well with the simulations obtained from single NWs, suggesting that interwire dipolar interactions are not strong. Nevertheless, the experimental loops measured along the long axis of the NWs are more sheared than the calculated ones, which is an indication of dipolar interactions.[21] The results clearly reveal that shape anisotropy dominates over magnetocrystalline anisotropy, also in accordance with the micromagnetic simulations. The finite coercivity is due to the non-zero magnetocrystalline anisotropy. By introducing non-magnetic Cu segments within the MSNWs, the magnetic easy axis can be modified and the M_r/M_s ratios can be tuned to the desired values, which is of importance for the subsequent magnetic manipulation of these NWs in fluids.

2.2.3. MFM Measurements on Single NWs

The surface topography image of three FeCo-rich NWs (two whole NW and one broken) is shown in Figure 5 **(**a**)**. The corresponding MFM image (Figure 5 (b)) reveals the remnant magnetization of the NWs, which creates a strong dipolar contrast. The MSNWs show a more complex remnant state than fully magnetic NWs. The topography and the corresponding MFM

image of two $FeCo_{150\ nm}/Cu_{150\ nm}$ MSNWs are shown in Figure 5 (c) and (d), respectively. The strength of the remnant stray magnetic field from the NWs is small compared to the fully magnetic NW case, as can be observed from the lower signal-to-noise ratio and the overall magnitude of the phase contrast in the MFM image. The alternating regions of contrast in the same nanowire indicate the presence of magnetic and non-magnetic segments along the NW. The MFM tip with the nominal coercivity of 400 Oe could magnetize the soft magnetic FeCo segments. The MFM image of these NWs shows that the introduction of non-magnetic segments in the NW architecture can clearly tune their overall magnetic domain pattern at remanence.

2.2. Magnetically Triggered Release Performance of MSNWs

In order to study the influence of magnetic tunability on the on-demand protein release performance, three types of NWs, namely non-magnetic (Cu-rich), fully magnetic (FeCo-rich), and $FeCo_{15\ nm}/Cu_{15\ nm}$ MSNWs, were selected. The release study was performed for each case as described in the experimental section. As presented in Figure 6, the release performance is found to depend on the total magnetization of the tested NWs. For non-magnetic Cu samples similar desorption results were detected irrespective of the presence of the magnetic field. In contrast, both magnetic FeCo-rich and MSNWs showed an increased BSA release when were subject to a magnetic field. The results provided in Figure 6 correspond well with the studies on attenuation of protein adsorption on oscillating CoNiFe NWs reported by Ainslie et al.[6] In this work, the authors show that protein release in the presence of an external oscillating magnetic field occurs due to the movement of the NWs resulting in shear modulated desorption. In our case, we evaluated the effect of reducing the amount of magnetic material within the NW architecture. For fully magnetic NWs the applied oscillating field increased protein release by 83%, whereas in

the case of $FeCo_{15\ nm}/Cu_{15\ nm}$ MSNWs protein release increased by 45%. When reducing by half the amount of magnetic material within the NW, the concentration of desorbed protein was decreased by approximately half. In this case, the NWs most probably exhibit less movement resulting in a smaller shear stress and thereby decreasing desorption.[6] However, one must point out that this behavior cannot be generalized for other macromolecules. Other compounds will exhibit different desorption performance due to their different affinity to metallic surfaces. In any case, the results suggest that protein release can be tuned by adjusting the architecture of the NWs. By combining arrays of fully magnetic NWs and MSNWs in the same platform, generation of complex concentration profiles and concentration gradients of biomolecules using external magnetic fields could be achieved. These preliminary studies suggest that these NWs can find applications in fields such as magnetic microfluidics and drug delivery in which concentration gradients are desired.

4. CONCLUSIONS

Multifunctional, magnetically tunable FeCo/Cu MSNWs were fabricated by pulse electrodeposition in AAO templates. By carefully controlling the deposition potential and time, it was possible to tune the segment composition and size. Various NWs with segment sizes ranging from 15 to 150 nm were achieved. The influence of non-magnetic Cu segments on the magnetization of NWs was investigated through VSM and MFM measurements. The results confirmed that the non-magnetic character of the Cu segments is crucial to tune the magnetic easy axis of the NWs. These findings match well with the simulations performed using Nmag software. The effect of magnetic tunability on the on-demand biomolecule release performance was investigated and the results revealed that the application of an external magnetic field could

be used to enhance the release of proteins on-demand. This phenomenon was observed prominently for fully magnetic FeCo NWs and was reduced for FeCo/Cu MSNWs. Thus, the results suggest that controlled drug release can be achieved by taking advantage of the magnetic architecture of the NWs. In conclusion, this study provides a compact nanosystem that is fully tunable and multifunctional.

ASSOCIATED CONTENT

Supporting information. MSNW morphology obtained when no complexing agent is present and summary containing the microstructural parameters of the different investigated NWs. This information is available free of charge via the Internet at http://pubs.acs.org/.

AUTHOR INFORMATION

Corresponding authors:

*E-mail: jordi.sort@uab.cat, vidalp@ethz.ch

Notes

The authors declare no competing financial interests.

ACKNOWLEDGMENTS

Dr. Salvador Pané acknowledges financial support by the European Research Council Starting Grant “Magnetoelectric Chemonanorobotics for Chemical and Biomedical Applications (ELECTROCHEMBOTS)”, by the ERC grant agreement n. 336456. Dr. Eva Pellicer and Prof.

Dr. Jordi Sort acknowledge 2014-SGR-1015 project from the Generalitat de Catalunya. Dr. Eva Pellicer is also grateful to MINECO for the “Ramon y Cajal” contract (RYC-2012-10839). The authors would like to acknowledge the Scientific Center for Optical and Electron Microscopy (ScopeM) of ETH Zürich for providing FIB SEM and TEM, and the FIRST laboratory for their technical support.

REFERENCES

(1) Hrkac, G.; Dean, J.; Allwood, D. A. Nanowire Spintronics for Storage Class Memories and Logic. *Philos. Trans. R. Soc., A* **2011**, *369*, 3214-3228.

(2) Fukami,S.; Yamanouchi, M.; Ikeda, S.; Ohno, H. Depinning Probability of a Magnetic Domain Wall in Nanowires by Spin-polarized Currents. *Nat. Comm.* **2013**, *4*, 1-7.

(3) Huang, H. T.; Ger T. R.; Lin, Y.H.; Wei, Z. H. Single Cell Detection Using a Magnetic Zigzag Nanowire Biosensor. *Lab Chip* **2013**, *13*, 3098-3104.

(4) Laocharoensuk R.; Bulbarello A.; Mannino S.; Wang J. Adaptive Nanowire-nanotube Bioelectronic System for On-demand Bioelectrocatalytic Transformations. *Chem. Commun.* **2007**, *28*, 3362-3364.

(5) Wang, J.; Scampicchio M., Laocharoensuk R.; Valentini R.; González-García O.; Burdick, J. Magnetic Tuning of the Electrochemical Reactivity through Controlled Surface Orientation of Catalytic Nanowires. *J. Am. Chem. Soc.* **2006**, *128*, 4562-4563.

(6) Ainslie, K. M.; Sharma, G.; Dyer M. A.; Grimes, C.; Pishko, M. V. Attentuation of Protein Adsorption on Static and Oscillating Magnetostrictive Nanowires. *Nano Lett.* **2005**, *5*, 1852-1856.

(7) Pereira A.; Palma, J. L.; Vázquez, M.; Denardinac J. C.; Escrig, J. A Soft/hard Magnetic Nanostructure Based on Multisegmented CoNi Nanowires. *Phys. Chem. Chem. Phys.* **2015**, *17*, 5033-5038.

(8) García, J.; Vega, V.; Iglesias, L.; Prida1, V. M.; Hernando, B.; Barriga-Castro, E. D.; Mendoza-Reséndez, R.; Luna, C.; Görlitz D.; Nielsch, K. Template-assisted Co–Ni Alloys and Multisegmented Nanowires with Tuned Magnetic Anisotropy. *Phys. Status Solidi* **2014**, *211*, 1041-1047.

(9) Sun, L.; Hao, Y.; Chien, C.-L.; Searson, P. C. Tuning the Properties of Magnetic Nanowires. *IBM J. Res. Dev.* **2005**, *49*, 79-102.

(10) Wang, H.; Patil, A. J.; Liu, K.; Petrov, S.; Mann, S.; Winnik, M. A.; Manners, I. Fabrication of Continuous and Segmented Polymer/Metal Oxide Nanowires Using Cylindrical Micelles and Block Comicelles as Templates. *Adv. Mater.* **2009,** *21*, 1805-1808.

(11) Callegari, V.; Demoustier-Champagne, S. Interfacing Conjugated Polymers with Magnetic Nanowires. *ACS Appl. Mater. Interfaces*, **2010**, *2*, 1369–1376.

(12) Tian, W.; Huang, L.; Zang, D.; Li, C.; Dang, J.; Wang, D. Segmented Polymer Nanowires and Nanorods by One-step Template Wetting with a Hyperbranched Polymer and Linear Polymer Blend. *RSC Adv.*, **2014**, *4*, 53021-53027.

(13) Park, D. H.; Hong, Y. K.; Cho, E. H.; Kim, M. S.; Kim, D.-C.; Bang, J.; Kim, J.; Joo, J. Light-Emitting Color Barcode Nanowires Using Polymers: Nanoscale Optical Characteristics. *ACS Nano*, **2010**, *4*, 5155-5162.

(14) Lee, J. H.; Wu, J. H.; Liu, H. L.; Cho, J. U.; Cho, M. K.; An, B. H.; Min, J. H.; Su Jung Noh, and Young Keun Kim. Iron–Gold Barcode Nanowires. *Angew. Chem. Int. Ed.*, **2007**, *46*, 3663-3667.

(15) Bakonyi, I.; Péter, L. Electrodeposited Multilayer Films with Giant Magnetoresistance (GMR): Progress and Problems. *Prog. Mater. Sci.* **2010**, *55*, 107-245.

(16) Péter, L.; Kupay, Z.; Cziráki, Pádár, J.; Tóth, J.; Bakonyi, I. Additive Effects in Multilayer Electrodeposition: Properties of CoCu/Cu Multilayers Deposited with NaCl Additive. *J. Phys. Chem. B*, **2001**, *105*, 10867-10873.

(17*)* Jang, B.; Pellicer, E.; Guerrero M.; Chen, X.; Choi H.; Nelson B. J.; Sort J.; Pané S. Fabrication of Segmented Au/Co/Au Nanowires: Insights in the Quality of Co/Au Junctions. *ACS Appl. Mater. Interfaces*. **2014**, *6*, 14583-14589.

(18) Gutfleisch, O.; Willard, M. A.; Brück, E.; Chen, C. H.; Sankar, S. G.; Liu, J. P. Magnetic Materials and Devices for the 21st Century: Stronger, Lighter, and More Energy Efficient. *Adv. Mater.* **2011**, *23*, 821-842.

(19) Hunter, D.; Osborn, W.; Wang, K.; Kazantseva, N.; Hattrick-Simpers, J.; Suchoski, R.; Takahashi, R.; Young, M. L.; Mehta, A.; Bendersky, L. A.; Lofland, S. E.; Wuttig, M.; Takeuchi, I. Giant Magnetostriction in Annealed $Co_{1-x}Fe_x$ Thin Films. *Nat. Commun.* **2011**, *2*, 1-7.

(20) Sahin, T.; Kockar, H.; Alper, M. Giant Magnetoresistance and Magnetic Properties of CoFe/Cu Multilayer Films: Dependence of Electrolyte pH. *J. Supercond. Novel Magn.* **2013**, *26*, 825-829.

(21) Zeeshan, M. A.; Pané, S.; Youn, S. K.; Pellicer, E.; Schuerle, S.; Sort, J.; Fusco, S.; Lindo, A. M.; Park, H. G.; Nelson, B. J. Graphite Coating of Iron Nanowires for Nanorobotic Applications: Synthesis, Characterization and Magnetic Wireless Manipulation. *Adv. Funct. Mater.* **2013**, *23*, 823-831.

(22) Fischbacher, T.; Franchin, M.; Bordignon, G.; Fangohr, H. A Systematic Approach to Multiphysics Extensions of Finite-Element-Based Micromagnetic Simulations: Nmag. *IEEE Trans. Magn.* **2007**, *43*, 2896-2898.

(23) Brenner, A. *Electrodeposition of Alloys. Principles and Practice.* Academic Press, New York and London 1963.

(24) Yokoi, M. Suppression Effect and Additive Chemistry. In *Copper Electrodeposition for Nanofabrication of Electronics Devices Nanostructure Science and Technology* 2014, Nanostructure Science and Technology Series, Springer: New York, 2014; pp 27-43.

(25) Haehnel, V.; Fähler, S.; Schaaf, P.; Miglierini, M.; Mickel, C.; Schultz, L.; Schlörb, H. Towards Smooth and Pure Iron Nanowires Grown by Electrodeposition in Self-organized Alumina Membranes. *Acta Mater.* **2010**, *58*, 2330-2337.

(26) Schlörb, H.; Haehnel, V.; Khatri, M. S.; Srivastav, A.; Kumar, A.; Schultz, L.; Fähler, S. Magnetic Nanowires by Electrodeposition Within Templates. *Phys. Status Solidi B* **2010**, *247*, 2364-2379.

(27) Jung, H. S.; Doyle, W. D.; Matsunuma, S. Influence of Underlayers on the Soft Properties of High Magnetization FeCo Films. *J. Appl. Phys.* **2003**, *93*, 6462-6464.

Table 1. Composition of FeCoCu electrolyte

Bath composition	Concentration (M)
Copper sulfate pentahydrate	0.00056
Cobalt sulfate heptahydrate	0.05
Iron sulfate heptahydrate	0.025
Ascorbic acid	0.025
Glycine	0.0125
Ammonium chloride	0.3
Boric acid	0.4
Sodium saccharinate	0.004
Polyethylene glycol (MW 400)	0.00088
pH	3

Table 2. Coercivity and reduced remanence values are presented for four different types of NWs.

Condition	H_c // (Oe)	H_c ⊥ (Oe)	M_r/M_s // (%)	M_r/M_s ⊥ (%)
$FeCo_{15nm}/Cu_{15nm}$	226	237	8	8
$FeCo_{100nm}/Cu_{15nm}$	311	323	25	18
$FeCo_{15nm}/Cu_{100nm}$	244	393	6	22
FeCo rich	184	214	6	8

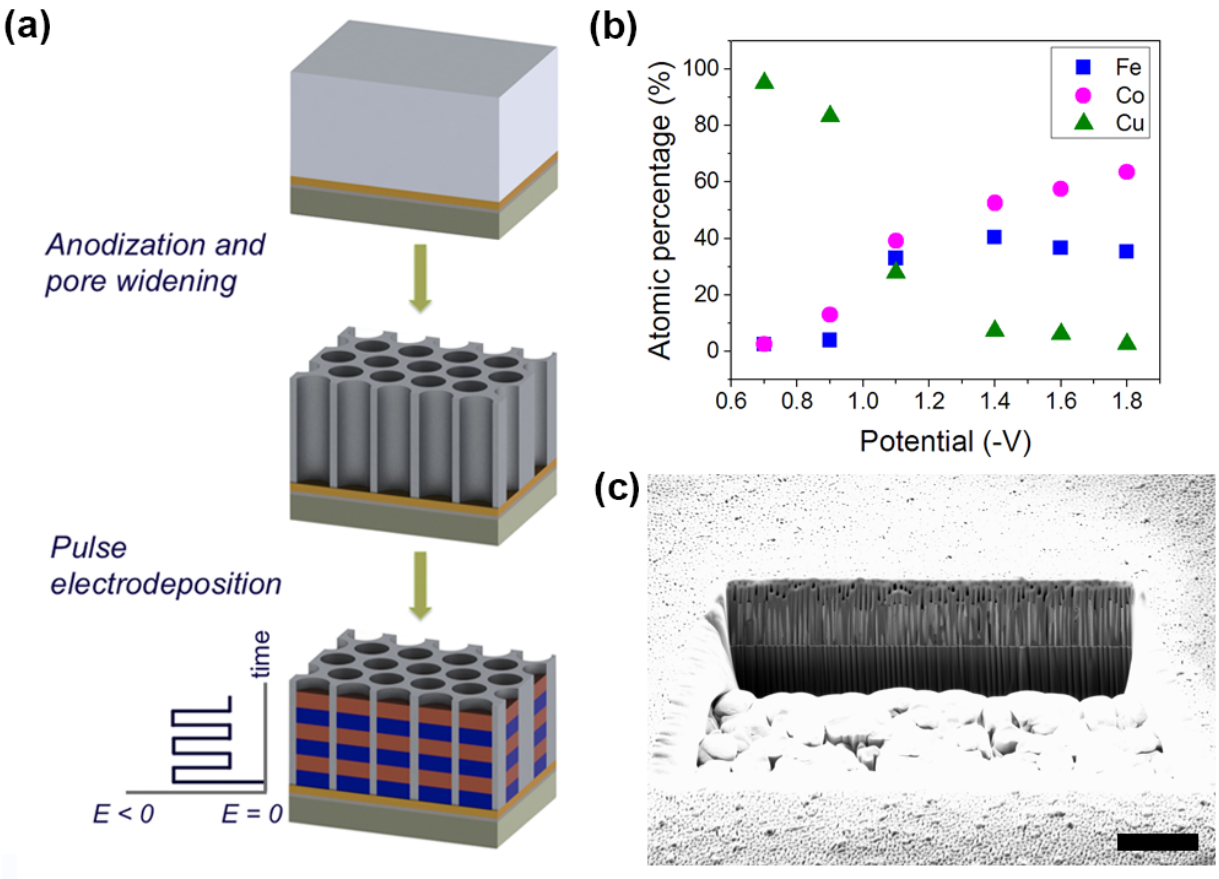

Figure 1. (a) Scheme of the fabrication process. First, anodization of evaporated Al on Au/Ti-coated Si substrates is performed. Next, a chemical treatment is realized in order to widen the pores. Subsequently, the MSNWs are electrodeposited in AAO templates by alternating the potentials for Cu-rich and FeCo-rich electrodeposition; b) Effect of the deposition potential on the composition of electrodeposited ternary alloy NWs; (c) Cross-sectional view of MSNWs embedded in the pores of an AAO template (scale bar shows 1 μm).

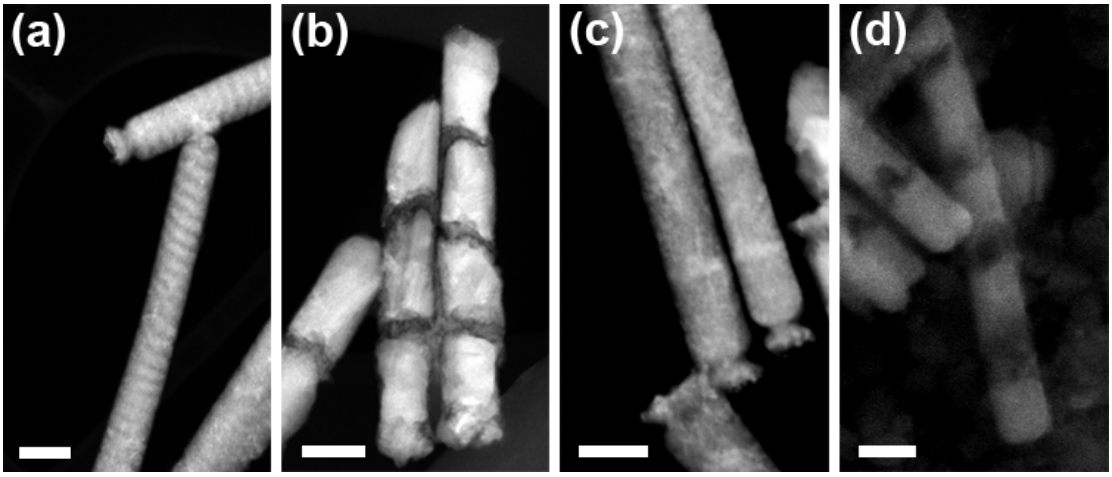

Figure 2. STEM/SEM images of MSNWs with different segment sizes grown by alternating the potential between -1.8 V and -0.7 V using the pulse times of (a) FeCo (0.5 s), Cu (15 s) (STEM); (b) FeCo (0.5 s), Cu (120 s) (STEM); (c) FeCo (3 s), Cu (15 s) (STEM), and (d) FeCo (4 s), Cu (120 s) (SEM) are shown. The bright segments correspond to Cu-rich phase whereas the dark segments show FeCo-rich phases. Scale bars show 100 nm. The total number of segments along the MSNWs per condition is (a) 64, (b) 8, (c) 16, and (d) 8, respectively.

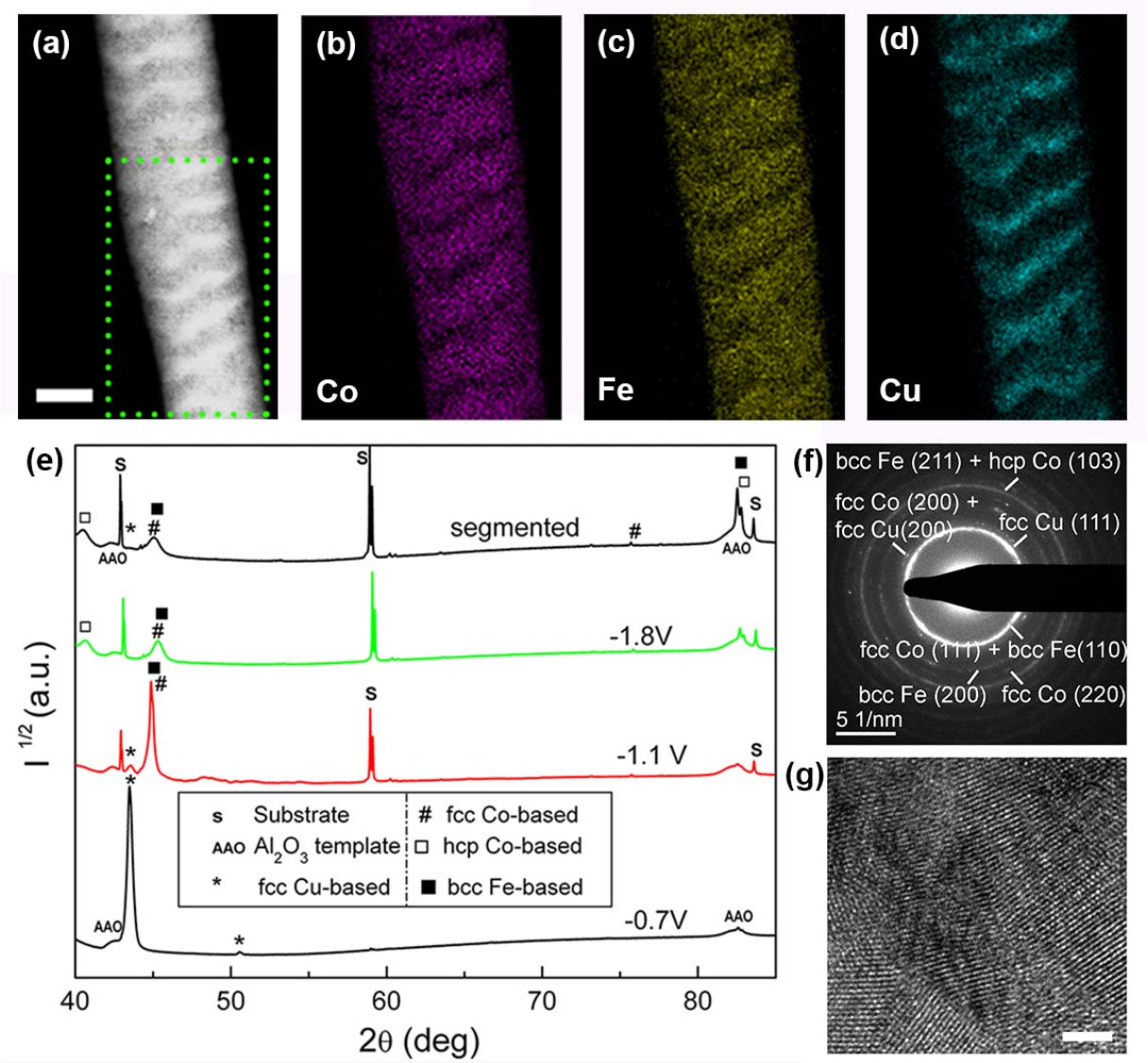

Figure 3. (a) STEM image of a $FeCo_{15\ nm}/Cu_{15\ nm}$ MSNW and the corresponding element distribution EDX mappings for (b) Co, (c) Fe, (d) Cu. Scale bar corresponds to 50 nm and the dotted lines in (a) correspond to the EDX mapping zone. Structural characterization results are also presented. (e) XRD patterns for FeCoCu ternary alloy NWs grown at -0.7 V, -1.1 V, -1.8 V and $FeCo_{15\ nm}/Cu_{15\ nm}$ MSNWs. The peaks indicated by an S are due to the substrate. Note that the broad halos corresponding to anodized aluminum oxide (AAO) are also indicated in the figure.

(f) SAED pattern taken from a $FeCo_{15\ nm}/Cu_{15\ nm}$ MSNW and (g) the related HRTEM image are shown (scale bar shows 2 nm).

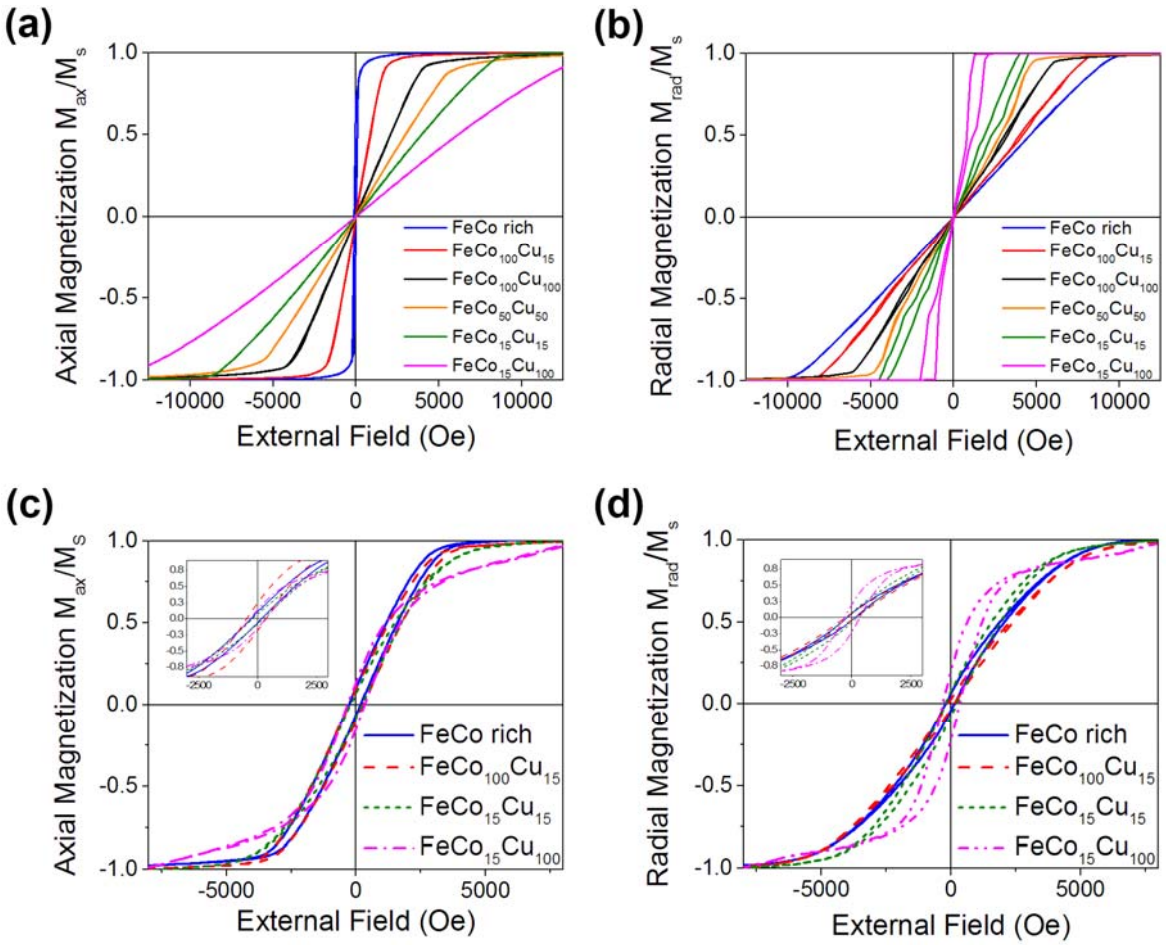

Figure 4. Micromagnetic simulations for the hysteresis loops of MSNWs are presented for (a) axial and (b) radial magnetization. Six different segment size conditions are shown. VSM measurements of selected MSNWs are given for (c) axial (parallel to NW long axis) and (d) radial (perpendicular to NW long axis) hysteresis loops. The results correspond to the MSNWs embedded in the alumina template.

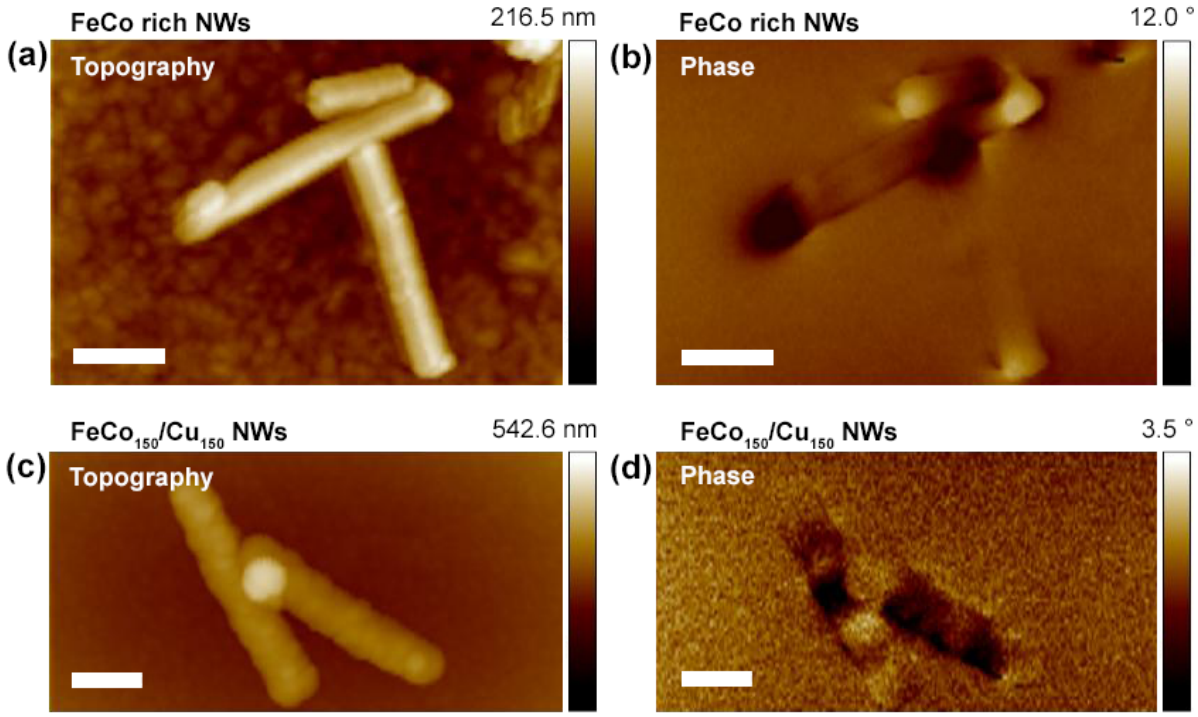

Figure 5. Atomic force microscopy (AFM) (left) and magnetic force microscopy (MFM) (right) images corresponding to (a), (b) FeCo-rich NWs and (c), (d) $FeCo_{150\ nm}/Cu_{150\ nm}$ MSNWs. Scale bars indicate 500 nm (a), (b) and 300 nm (c), (d).

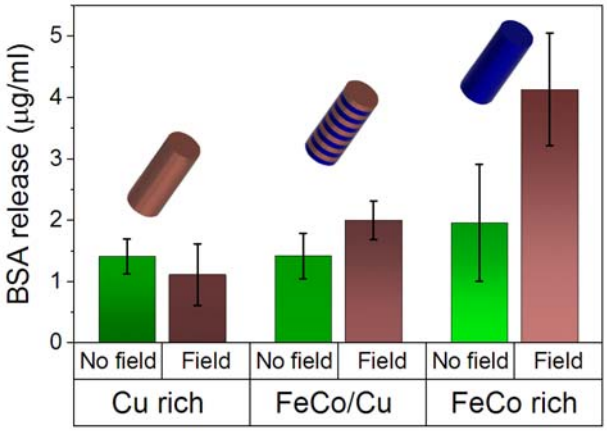

Figure 6. BSA release amount for the three studied NW conditions is shown. The schematic NWs are for Cu-rich, segmented $FeCo_{15\ nm}/Cu_{15\ nm}$, and FeCo-rich NWs.

Table of Contents

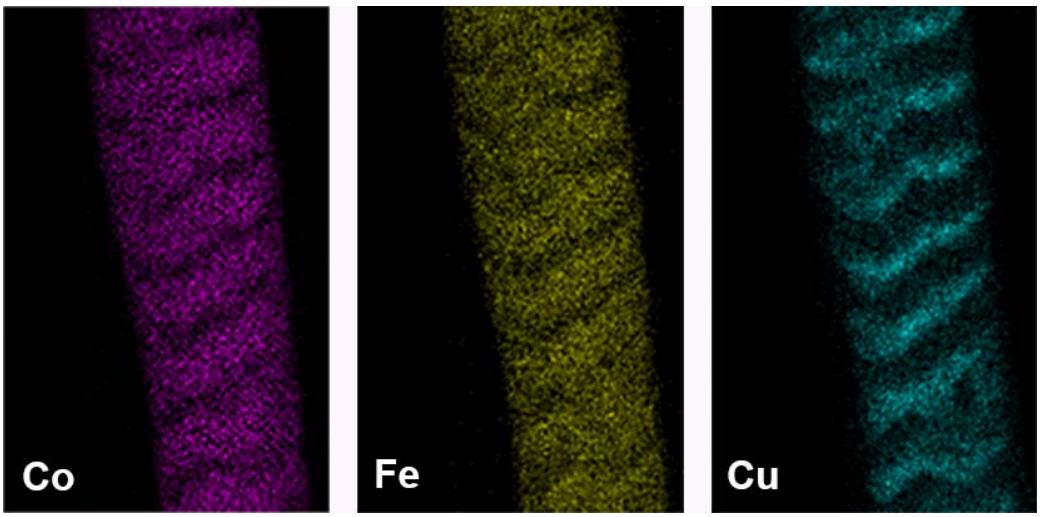

SUPPORTING INFORMATION

Multisegmented FeCo/Cu nanowires: electrosynthesis, characterization and magnetic control of biomolecule desorption

Berna Özkale,[§] Naveen Shamsudhin,[§] George Chatzipirpiridis,[§] Marcus Hoop,[§] Fabian Gramm,[□] Xiangzhong Chen,[§] Xavi Martí,[ξ] Jordi Sort,[‡,] Eva Pellicer,[†] and Salvador Pané[§,*]*

[§] Multi-Scale Robotics Lab (MSRL), Institute of Robotics & Intelligent Systems (IRIS), ETH Zürich, Zürich 8092, Switzerland

[□] Scientific Center for Optical and Electron Microscopy (ScopeM), ETH Zürich, Zürich 8093, Switzerland

[ξ] Department of Spintronics and Nanoelectronics, Institute of Physics ASCR, v.v.i., Cukrovarnická 10, 162 53 Praha 6, Czech Republic

[‡] Institució Catalana de Recerca i Estudis Avançats (ICREA) and Departament de Física, Universitat Autònoma de Barcelona, Campus UAB, Bellaterra, 08193 (Spain)

[†] Departament de Física, Facultat de Ciències, Universitat Autònoma de Barcelona, Campus UAB, Bellaterra 08193, Spain

* Corresponding authors: sort.jordi@uab.cat, vidalp@ethz.ch

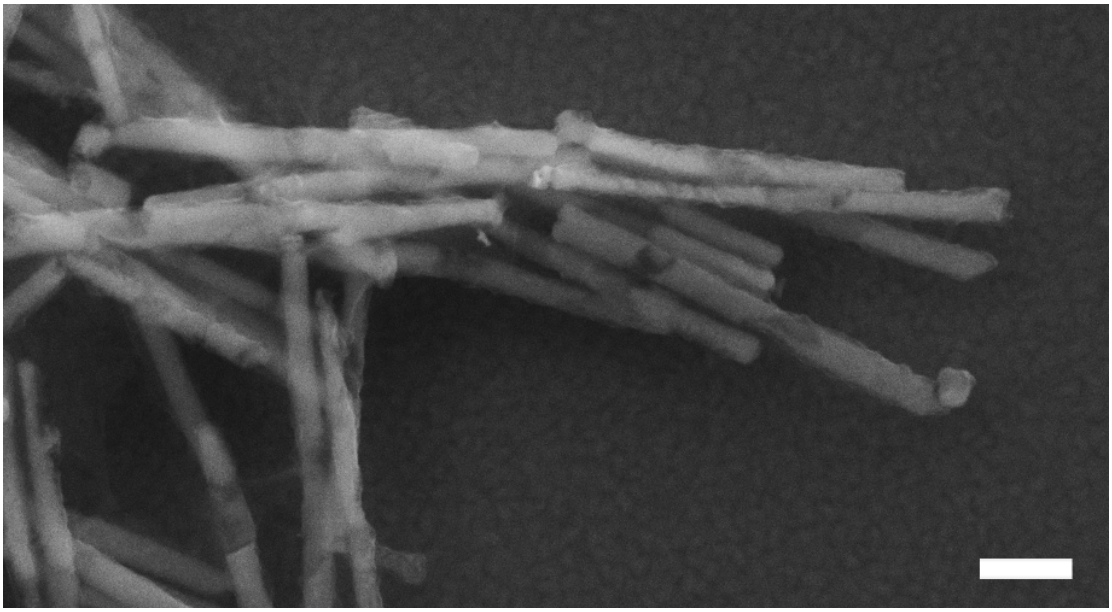

Figure S1. MSNW architecture obtained when the complexing agent, glycine, is not present in the electrolyte (scale bar is 300 nm). The MSNWs exhibit irregular morphology and segment sizes when the electrolyte lacks the complexing agent.

Table S1. Summary of the microstructural parameters of the different investigated NWs. Note that the tabulated lattice parameters of pure fcc-Co, pure fcc-Cu and pure bcc-Fe are a = 3.5447 Å, 3.6150 Å and 2.8665 Å, respectively, whereas those of pure hcp-Co are a = 2.5031 Å and c = 4.0605 Å.[1] The differences between tabulated and experimental values indicate the formation of solid solutions.

		Ternary NWs -0.7V	Ternary NWs - 1.1V	Ternary NWs -1.8V	MSNWs
fcc Cu-rich	a (Å)	3.5967	3.5903	-	-
	<D> (nm)	60	50	-	-
	$(\varepsilon^{1/2})^2$	0.00013	7.9×10^{-4}	-	-
fcc Co-rich	a (Å)	-	3.4795	3.5270	3.5292
	<D> (nm)	-	55	32	35
	$(\varepsilon^{1/2})^2$	-	5×10^{-5}	0.00129	0.00013
hcp Co-rich	a (Å)	-	-	2.5561	2.5461
	c (Å)	-	-	4.0110	4.01305
	<D> (nm)	-	-	40	40
	$(\varepsilon^{1/2})^2$	-	-	0.0051	0.00321
bcc	a (Å)	-	2.8609	2.8325	2.8387

Fe-rich	<D> (nm)	-	25	35	42
	$(\varepsilon^{1/2})^2$	-	3×10^{-5}	0.00366	0.00459

(1) PDFWIN Software (JCPDS-ICDD).